

Composition and structure control of ultralight graphene foam for high-performance microwave absorption



Yi Zhang, Yi Huang^{*}, Honghui Chen, Zhiyu Huang, Yang Yang, Peishuang Xiao, Ying Zhou, Yongsheng Chen^{**}

Centre for Nanoscale Science and Technology, Key Laboratory of Functional Polymer Materials, Collaborative Innovation Center of Chemical Science and Engineering (Tianjin), School of Materials Science and Engineering, Nankai University, Tianjin, 300071, China

ARTICLE INFO

Article history:

Received 18 February 2016
Received in revised form
21 April 2016
Accepted 27 April 2016
Available online 28 April 2016

ABSTRACT

Macroscopic lossy foam has been expected to be the most promising candidate for lightweight high-performance microwave absorption (MA). However, inferior MA behaviors of conventional foams reported previously are disappointing. The emerging graphene foam (GF) has broken this paradoxical state of affairs. Here, series of GFs with various chemical compositions and physical structures have been prepared via a facile and controllable method and their MA performance is investigated in 2–18 GHz. The in-depth analyses of the GF's composition, structure and MA property demonstrate that the MA performance of the GF is strongly correlated with the C/O ratio, conjugated carbon domain size and graphene framework's microstructure. A maximum absorption value of -34.0 dB as well as 14.3 GHz qualified bandwidth with reflection loss below -10 dB is achieved for the GF with an ultralow bulk density of 1.6 mg/cm³, of which the average absorption intensity and the specific MA efficiency are much higher than those of the best available MA materials in previous literature. The composition & structure–performance relationship of MA foams is revealed. The balance between small interfacial impedance gap and high loss characteristic has wide implications in improving the MA performance of the GF and other porous materials.

© 2016 Elsevier Ltd. All rights reserved.

1. Introduction

With the rapid arising of information technology, microwave absorption materials are playing an increasingly significant role in electronic reliability, healthcare, and national defense security [1–4]. For example, the microwave absorption (MA) materials applied in the emerging high-speed communication apparatus like satellites could improve the receiver's signal quality by suppressing the noise [5]. Besides, MA materials in the radar station and the relay station could protect inside workers from overdose exposure to high-power microwave [6]. Most importantly, with the gradual maturation of novel advanced anti-stealth radars such as ultra wide band radar, phased array radar, multi-static radar and passive radar, high-performance counter-detection MA materials serve as a very efficient route in increasing the survivability of military units via

reducing their radar cross-section [7]. The ideal MA materials are primarily required to establish an excellent double-win relationship between intense absorption ability and broad absorption bandwidth. In addition, MA materials with ultralight weight and thin thickness will be advantageous in the fields of aerospace, aviation, ground vehicles and fast-growing next-generation green miniature electronics [1,8,9].

The interfacial impedance gap and radiation energy loss characteristics are considered as the two core principles that determine the MA performance of a material [10–13]. The microwave propagation for a typical homogenous material's MA process depends on several factors, including dielectric permittivity ϵ , magnetic permeability μ and electrical conductivity δ , which are a comprehensive reflection of significant component and structural characteristics [4,14–16].

For decades, researchers have made considerable efforts towards designing and fabricating various MA materials by adjusting the electrical conductivity, dielectric constant and magnetic permeability in the pursuit of low interfacial impedance gap as well as high loss ratio of incident microwave [10,11,13,17,18]. In

^{*} Corresponding author.

^{**} Corresponding author.

E-mail addresses: yihuang@nankai.edu.cn (Y. Huang), yschen99@nankai.edu.cn (Y. Chen).

most cases, separate solid particle absorbents, such as ferrites [19,20], metal powders [20,21], ceramics [22], carbon nano/micromaterials [23,24] and their hybrids [2,15,25,26], are extensively adopted as fillers into microwave-transparent organic or inorganic adhesives to fabricate MA composites. Besides mediocre MA performance, most of them have also been kept far from practical application for some shortcomings, such as high density, poor stability and large loading content [1,12,27]. It has been demonstrated, for instance, 70 wt% or more magnetic iron particles with a very high density of 8 g/cm³ are required in typical MA composites [17,20].

Three-dimensional (3D) macroscopic porous lossy materials have been expected to be the most promising candidate for lightweight high-performance broadband MA application [28–32]. Compared with conventional uniform solid MA materials, the MA foam, with so many homogeneously-dispersed internal pores, not only shows lower bulk density but also gives much smaller effective permittivity, which makes it less resistive to the detectable incident microwave in a wide frequency range [16,33]. Until now, considerable attentions have been paid to synthesis and application of porous bulk materials for microwave suppression, such as conductive polymer foam [28,34,35], silicon carbide foam [36,37], carbon foam [7,29,38,39] and carbon nanotube sponge [40]. However, for most MA foams reported previously, their MA behaviors could not be compared with those of traditional solid MA materials [7,35,36]. Furthermore, it is still a big challenge to reveal the composition & structure–performance relationship of MA foams due to their complicated irregular structures and preparation techniques, which severely hinders their practical application.

Recently, significant progress toward 3D macroscopic interconnected graphene networks has opened up a new route for the exploitation of porous bulk material for lightweight and broadband high-performance MA application [38,41–49]. In the previous communication, we preliminarily proved the outstanding microwave absorbing performance of macroscopic GFs, which showed that GFs may have great potential in MA application [32]. However, there remains much uncertainty in the GF's MA property dependence on its morphology and composition. Therefore, it is very significant to develop a facile and controllable method to prepare additive-free large-sized GFs and establish the relationship between the MA property and the GF's intrinsic structure and component, which is essential in an in-depth understanding of its MA mechanism and more importantly developing a universal strategy to effectively enhance the MA property of bulk porous materials.

Herein, we demonstrate design and fabrication of various GFs with different internal morphologies and compositions and investigate their MA performance in 2–18 GHz, which is intensively occupied for satellite communications, remote sensing, radar detections and weapons guidance and tracking. The MA performance of the GF foam is found to be strongly correlated to the C/O ratio, sp² carbon domain size and graphene framework microstructure. A maximum absorbing value of –34.0 dB as well as 14.3 GHz qualified bandwidth can be obtained for the GF with an ultralow density of 1.6 mg/cm³, which is close to the density of ambient air (1.2 mg/cm³) and much lower than those of the carbon foam (166 mg/cm³) [29] and the SiC foam (~256 mg/cm³) [37]. More importantly, the GF presents the best average absorption intensity compared with other typical MA materials in 2–18 GHz. The specific MA efficiency is nearly two orders of magnitude higher than those of the best available MA materials ever reported. The mechanism for the MA performance dependence on the composition and structure of the GF is revealed. The well-matched interfacial impedance combined with high loss ability gives rise to the enhanced MA performance.

2. Experimental

2.1. Synthesis of GF

The raw material, single-layer graphene oxide (GO), was prepared using a modified Hummers method as described elsewhere and has the lateral size mainly above 10 μm [42]. The initial concentrated GO ethanol solution was diluted into three GO ethanol reaction solutions with concentrations of 0.3, 0.6 and 0.9 mg/mL, respectively. After solvothermal reaction, solvent exchange and freeze drying, three original GFs with different graphene volume fractions were obtained. The GFs made from 0.3 to 0.9 mg/mL GO ethanol solutions were annealed at 600 °C for 1 h in argon at ramp rate of 10 °C min⁻¹ to obtain the target GFs labeled as C0.3 and C0.9, individually. The remaining GFs starting from 0.6 mg/mL GO solution were divided into five small batches, four of which were annealed at different temperatures of 200, 400, 600 and 800 °C for 1 h in argon at ramp rate of 10 °C min⁻¹ separately to obtain the target GFs with different compositions. The unannealed GF is marked as T0 and the annealed products are marked as T200, T400, T600 and T800 in ascending temperature sequences. For convenience, the sample T600 is also named C0.6 in the GF's structure comparison. To further study the GF's MA property dependence on its interconnected conductive network of graphene sheets, some of the sample C0.6 was broken into powders via mechanical stirring at 1800 rpm.

2.2. Characterization

The Raman spectrum of the GF was obtained on a Renishaw inVia Raman spectrometer using laser excitation at 514.5 nm. The X-Ray diffraction (XRD) measurement of the GF was carried out on a Rigaku D/Max-2500 diffractometer with Cu Kα radiation. The morphology of the GF was observed by Scanning Electron Microscopy (SEM) (LEO 1530VP operated at 3.0 kV). The electrical conductivity of the GF was measured by a homemade fixture as previously reported. The Transmission electron microscopy (TEM) investigation was performed on a FEI Tecnai G² F20 operated at 200 kV. The thermogravimetric analysis was obtained using a NETZSCH STA 409 PC analyzer, with a heating rate of 10 °C min⁻¹ from room temperature to 850 °C in the air. The X-ray Photoelectron Spectroscopy (XPS) was examined with a GENESIS 60S X-ray photoelectron spectrometer using an Al Kα (hν = 1486.6 eV) radiation and the binding energies were calibrated by using the containment carbon peak (C1s = 284.6 eV). After all GFs were dried in vacuum at 75 °C for 24 h, their Fourier transform infrared (FT-IR) spectra and combustion elemental analysis were then investigated at Tensor 27 FT-IR Spectrometer (Bruker, Germany) and Vario micro elemental analyzer (Elementar, Germany), respectively.

Based on the Arch method, the MA performance was evaluated in 2–18 GHz using an Agilent HP8757E scalar quantity network analyzer. Four GFs cut into 90 mm × 90 mm × 10 mm were arranged into a cubic container with internal dimensions of 180 mm × 180 mm × 15 mm for measurements in the frequency band of 2–18 GHz. The powder sample with a mass equivalent to the MA test sample C0.6 was loosely placed in the container for the MA measurement. All GFs were backed with a highly conductive aluminum plate to reflect the entire incident microwave back to the receiving antenna.

The relative complex permittivity and permeability were measured in the frequency range of 2–18 GHz using an Agilent HP8722ES vector network analyzer. Paraffin was used as the supporting matrix due to its minor complex electromagnetic parameters approximating those of air. The toroidal test sample (3 mm i. d., 7 mm o. d. and 2 mm thickness) was fabricated by vacuum-

impregnating the GF with paraffin. The incident microwave direction was perpendicular to the test sample.

3. Results and discussion

3.1. The dependence of MA performance on the GF's chemical composition

The macroscopic additive-free GF for MA tests was prepared mainly through a solvothermal reaction, followed by solvent removal and thermal reduction. By varying annealing temperatures in the thermal reduction from room temperature to 800 °C, five types of pie-shaped GFs starting from the same GO concentration of 0.6 mg/mL were obtained to study the MA performance dependence on the chemical composition. For convenience, the unannealed GF is labeled as T0 and the other annealed products were labeled as T200, T400, T600 and T800 in temperature sequences. Due to the pyrolysis of the labile oxygen-containing groups and the carbon defects, the GF undergoes an obvious weight loss during the thermal reduction. As shown in Fig. 1a, the GF's bulk density declines by over 50% with the annealing temperature rising from room temperature to 800 °C. Given the low intrinsic density of graphene sheets, the porosity higher than 99% can be obtained for five types of GFs, exceeding those of most macroscopic foams [29–31,43].

To understand chemical composition transformation of the GF annealed at different temperatures, elemental analysis, XPS, Raman spectroscopy and thermogravimetric analysis were performed for every sample.

Elemental analysis offers the most direct evidence for the element component of the GF sample. Free of additives, all the GF samples are mainly composed of carbon and oxygen as same as the initial GO. As shown in Fig. 1b, the unannealed GF T0 has the highest oxygen content, indicative of its most severely damaged conjugated carbon backbones. As the annealing temperature rises, the carbon content grows continuously, which is opposite for the

oxygen content in the GF sample. Even for the GF annealed at 800 °C, the existence of oxygen manifests that it serves as the tough bonding element in chemically linking adjacent graphene sheets, ensuring the thermally reduced GF's robust mechanical strength. It should be noted that the C/O ratio increasing trend clearly accelerates upon the annealing temperature rising to 400 °C, which may result in an abrupt change in the GF's MA property.

The FT-IR spectra for the GF samples with various chemical compositions are shown in Fig. 1c. The absorption peaks appear at 1730, 1570 and 1220 cm^{-1} , corresponding to the C=O stretching mode, C=C stretching vibration of benzene ring and breathing vibration mode of the C–O groups, respectively and the broad peak at 3400 cm^{-1} is attributed to the adsorbed water in the sample due to the GF's high porosity [42]. With the annealing temperature increasing, the C=O stretching vibration peak gradually attenuates and nearly vanishes at 800 °C. Remarkably, the everlasting C–O breathing vibration peak, on the one hand, demonstrates that the mutually entangled graphene sheets are chemically reinforced by the C–O–C covalent bond analogues. On the other hand, such defects, considered as the polarization domains, contribute to improving the microwave-absorbing ability of the GF [11,12].

In the Raman spectra (Fig. 1d), all the GF samples display two evident peaks at 1351 cm^{-1} and 1588 cm^{-1} , corresponding to the D and G bands respectively. The I_D/I_G ratio is associated with defect concentration of graphitic carbon materials [48]. It can be seen that with raising annealing temperature, the I_D/I_G ratio reduces dramatically from 0.95 for T0 to 0.76 for T800, which demonstrates the enlargement of sp^2 carbon domain. More precise analyses of in-plane conjugated carbon structures were conducted via XPS characterization (Fig. S1). Besides the main sp^2 carbon peak locating at 284.5 eV, the high-resolution C1s region of the GF can be divided into 4 other fitting peaks at 285.8 eV, 286.7 eV, 287.7 eV and 288.8 eV, which are attributed to carbon species of sp^3 carbon, C–O–C, C=O and C(C=O)O, individually [42]. The sp^2 conjugated carbon skeleton accounts for the vast majority of carbon species in all of the GF samples. Further semi-quantitative analyses (Fig. 1e)

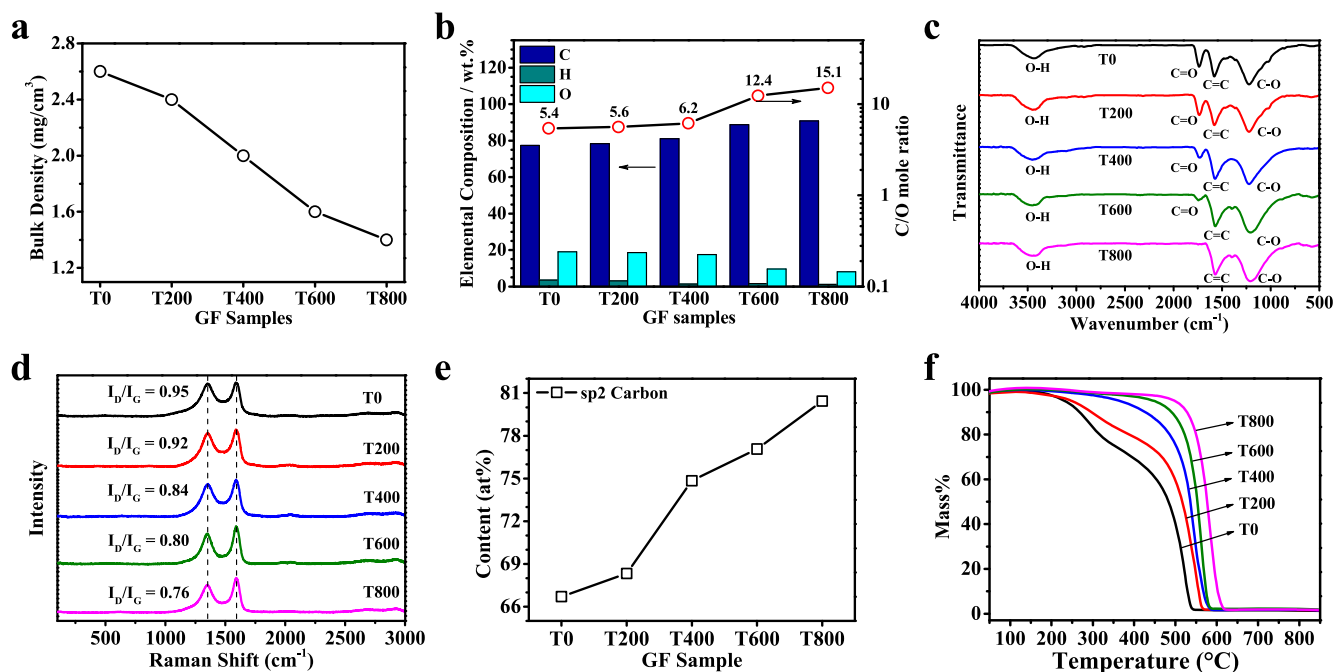


Fig. 1. (a) The bulk densities, (b) the elemental analysis, (c) the FT-IR spectra, (d) the Raman spectra, (e) the semi-quantitative sp^2 carbon domains analyses and (f) the thermogravimetric curves for the GFs annealed at different temperatures. (A colour version of this figure can be viewed online.)

prove that with the reduction temperature lifting to 800 °C this proportion keeps rising from 66.7 at% to 80.4 at% in the range from 200 °C to 400 °C which obviously grows fastest.

Thermogravimetric analyses (Fig. 1f) were performed to examine the composition thermostability of various GF samples. Both T0 and T200 appear apparent weight loss when the temperature approaches 200 °C. However, when the annealing temperature goes above 400 °C, the resulting GFs could maintain stable in air at operating temperature of over 300 °C. Due to the higher thermostability of sp² carbon backbones than those of oxygen-containing groups, these results suggest more conjugated carbon domains in the GFs annealed at higher temperature, which are consistent with the results of elemental analyses and XPS analyses. Additionally, the excellent thermostability makes such GFs suitable for applications at high temperature such as the skins of high-speed aircrafts and hoods of vehicle engines [50].

The qualified MA intensity for most applications is generally –10 dB [15,26]. Fig. 2 exhibits the reflection loss (RL) curves for GFs via different thermal treatments in the range of 2–18 GHz. With the C/O ratio as low as 5.4 and only 66.7% sp² carbon content, the original unannealed GF (T0) exhibits very inferior microwave-absorbing ability in the test frequency band owing to severe disruption of in-plane conjugated structures. Although the C/O ratio of T200 increases a little after the low-level thermal reduction, such poor restoration of its damaged conjugated graphene network does not make its RL curve differ obviously from that of T0. After the annealing temperature rising to 400 °C, there appears a significant improvement in the GF's MA performance. For T400, the strongest RL reached –28.4 dB at 13.9 GHz and the qualified frequency ranges from 5.6 GHz to 16.9 GHz. The phenomenon demonstrates that with the C/O ratio and sp² carbon domain over 6.2 and 74% respectively, the GF's partially recovered 3D porous conductive network of graphene sheets becomes sensitive to the incident microwave. T600 shows the optimal MA performance. In addition to the maximum RL of –34.0 dB at 13.1 GHz, its qualified frequency bandwidth reaches 14.3 GHz, covering 89.4% of the entire measured bandwidth, which is much wider than those of most MA materials reported previously [7,8]. With annealing temperature arising continuously, the change of the GF's MA performance doesn't maintain a monotonic evolution. On the contrary, upon the temperature surpassing 600 °C, the GF's MA property starts weakening, which suggests that with the C/O rising more than 12.4, over-restored conjugated carbon framework will increase the

reflection of the microwave and becomes harmful for the GF's MA property. Therefore, there exists an optimal reduction temperature, such as 600 °C in this case, under which the annealed graphene skeleton with certain C/O ratio and conjugated carbon domain size exhibits the best wave-absorbing ability.

3.2. The dependence of MA performance on the GF's physical structure

The material's microwave absorbing properties rely on not only the chemical composition, but also the physical structure, especially the basic absorbent's morphology and the interfacial microstructure [3,17,18]. A facile and controllable method is developed to fabricate GFs with controllable microstructure. Via adjusting GO concentration of the initial GO concentration from 0.3 to 0.9 mg/mL, three kinds of GFs annealed at the same temperature of 600 °C were prepared, which are marked as C0.3, C0.6 and C0.9 in ascending GO concentration for convenience.

Fig. 3a shows the bulk densities of three GFs with different physical structures. With the original GO ethanol solution getting denser, the resulting GF's density rises from 0.9 to 2.4 mg/cm³. The higher graphene content results in the weaker GF's liquid absorption capability (Fig. 3b), which is a direct reflection of the decrease in the GF's porosity [38,42]. However, similar to those of our other GFs, the calculated graphene volume fraction for all the three GF samples still keeps below 1%, which to some extent can be regarded as a stable individual characteristic of the additive-free 3D cross-linked network of graphene sheets.

Fig. 4 gives the SEM images of the GFs made from the GO solutions with different initial concentration. As can be seen, the starting GO concentration has a great impact on the internal porous morphology and cell size of the resulting GF. When the starting solution contains very few GO sheets (0.3 mg/mL), the resulting GF shows a reticulum-like open cell structure with the pore size ranging from 30 to 90 μm, in which most graphene sheets concentrate on the edge and form the struts with many enclosed walls incompletely. Upon raising the GO concentration of the starting solution to 0.6 mg/ml, the GF with negligible change in its internal pore size, experiences an enormous morphological evolution from the open reticular structure to the semi-closed cellular one with much more complete cell walls. As the initial GO concentration keeps rising to 0.9 mg/mL, the GF internal pores begin shrinking distinctly. It is worth noting that although its long-range network has been broken, the C0.6 powder still presents an intricate 3D interconnected graphene network with tremendous micro-sized polygon pores like other intact GFs, which further demonstrates the robust mechanical property of the 3D monolithic structure.

As we have pointed out, the interfacial microstructure of the absorbent will exert significant impact on the microwave lossy propagation in the MA material [19,32,48]. Therefore, we further investigate the influence of graphene content on the GF' cell wall via TEM characterization (Fig. 5a–c). C0.3's cell wall is comprised of 1–5 layer graphene sheets with poor restacking, which should be most beneficial to the transmission of the incident microwave through the whole foam. With the increasing of the GO content in the starting solution, the GF's cell walls gradually become thicker. Upon raising GO concentration to 0.9 mg/mL, the GF even presents some internal cell walls consisting of as high as 8–14 layer graphene sheets, over twice the thickness of the GF with the lowest initial GO content.

To further characterize internal structure of the GF, the X-ray diffraction (XRD) examination of various GFs made from different GO solutions were performed with flake graphite as the comparison (Fig. 5d). Different from the strong sharp peak for graphite at

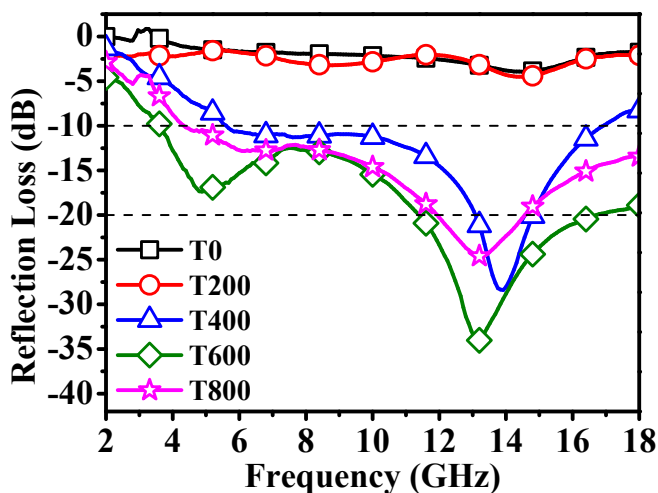


Fig. 2. The RL curves for the GFs with different chemical compositions in 2–18 GHz. (A colour version of this figure can be viewed online.)

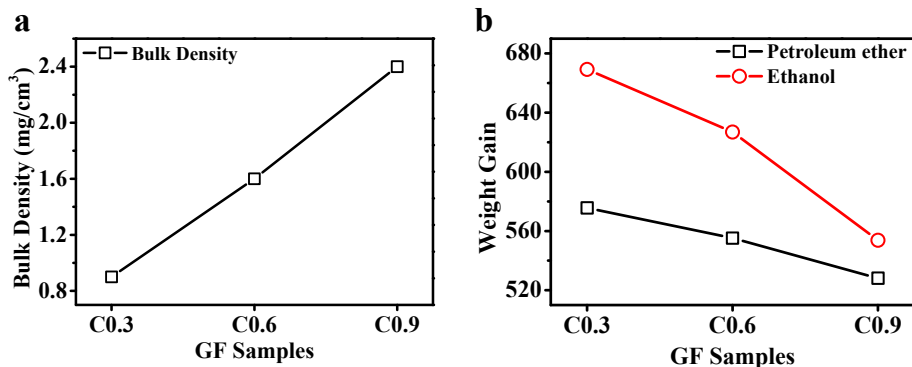


Fig. 3. (a) The bulk density and (b) the liquid absorption capabilities of the GFs. (A colour version of this figure can be viewed online.)

$2\theta = 26.5^\circ$, all the GFs exhibit rather broad feeble peaks (002), indicating that the long-range restacking of graphene sheets is very weak. Note that as the initial GO concentration moves up, additional wide weak peaks at 25.0° and 25.9° emerge for C0.6 and C0.9, respectively. The result proves that C0.6 and C0.9, with more graphene constituent, possess more restacking structures than C0.3, which is consistent with the TEM characterization.

The RL curves for all the GF samples in 2–18 GHz are shown in Fig. 6. The GF made from the 0.3 mg/mL GO solution displays the weakest wave-absorbing ability with the maximum absorption intensity of -15.0 dB at 18.0 GHz and the qualified bandwidth of 6.0 GHz. With the initial GO increasing from 0.3 mg/cm³ to 0.6 mg/cm³, a maximum RL of -34.0 dB is achieved at 13.1 GHz. More significantly, the qualified frequency bandwidth (14.3 GHz) improved dramatically, covering most of the entire measured bandwidth. With the further increasing of the concentration of GO solution, the GF exhibits a reduced microwave absorbing ability. The result indicates that there exists an optimal initial GO concentration that makes the self-assembled GF possess the best MA performance and this value is most approximate to 0.6 mg/mL in our case. It should be noted that the variance for all the GF samples in graphene volume fraction does not surpass 1%, which demonstrates that the GF's MA performance is much sensitively affected by its physical structure. Furthermore, compared to other unbroken GFs, the GF powder exhibit a very poor MA performance with the narrow qualified bandwidth of 1.4 GHz and low optimal absorption strength of -11.5 dB. The experimental result indicates that the highly intricate interconnected long-range conductive network is imperative to the excellent MA property of the GF.

3.3. Comparison of the GF's comprehensive MA performance with other MA materials

The detailed MA performance of some representative MA materials reported before is listed in Table S1 for comparison. It can be seen that the optimized GF exhibits much more excellent MA performance both in the maximum absorbing intensity and in the qualified bandwidth than most MA materials, including the MA foams. Because of the great importance of the absorbing intensity throughout quite a broad frequency range in the broadband high-performance MA research, it's necessary to introduce a new concept of the average absorption intensity (AAI) which is analogue to External Quantum Efficiency in the photovoltaic field. The AAI is expressed as

$$AAI(\text{dB}) = \frac{\left| \int_{f_l}^{f_h} (RL) df \right|}{f_h - f_l} \quad (1)$$

where f_l and f_h respond to the lowest measured frequency and the highest measured frequency, respectively. The higher the AAI value is, the stronger broadband microwave absorbing ability the material presents. The AAI in 2–18 GHz of several representative MA materials in previous literature were calculated in Fig. 7a. Owing to the strong microwave absorbing behavior in the wide frequency band, the GF shows a very excellent AAI (17.9 dB), which is higher than the best available MA materials reported previously.

Furthermore, light weight accounts for a giant proportion in designing and evaluating microwave attenuation materials applied in aerospace, aviation and ground vehicles [9,35]. Therefore, we adopt the specific MA efficiency (SMAE) integrated with significant MA indicators such as thickness, density, qualified bandwidth and RL values in the measured frequency band to evaluate the microwave absorption (MA) performance more comprehensively [32]. The SMAE is expressed as

$$SMAE(\text{dB} \cdot \text{Hz} \cdot \text{cm}^2 \cdot \text{g}^{-1}) = \frac{\left| \int_{f_l}^{f_h} (RL) df \right|}{t \cdot \rho_{\text{bulk}}} \quad (2)$$

where f_l , f_h , t and ρ_{bulk} respond to the lowest qualified frequency, the highest qualified frequency, the average thickness and the average bulk density of the MA material, respectively. A material with high SMAE is anticipated to have a huge potential in MA application. The specific MA efficiency in 2–18 GHz of several representative MA materials in open literature were calculated in Fig. 7b. Despite of the low bulk density, the specific MA efficiency of the carbon foam [7] and SiC foam [37] don't go over $100 \text{ dB Hz cm}^2 \text{ g}^{-1}$, which is much inferior to some typical solid MA material, such as the SWNT/polyurethane composite ($\sim 1.5 \times 10^2 \text{ dB cm}^2 \text{ g}^{-1}$) [8], the reduced GO/NBR composite ($\sim 2.2 \times 10^2 \text{ dB Hz cm}^2 \text{ g}^{-1}$) [23] and the α -Fe encapsulated within carbon nanotube/epoxy composite ($\sim 2.0 \times 10^3 \text{ dB Hz cm}^2 \text{ g}^{-1}$) [15]. Remarkably, the excellent MA performance combined with the ultralow density (1.6 mg cm⁻³) gives the optimized GF a superior specific MA efficiency around $1.7 \times 10^5 \text{ dB cm}^2 \text{ g}^{-1}$, nearly two orders of magnitude higher than those of the best available MA materials reported before.

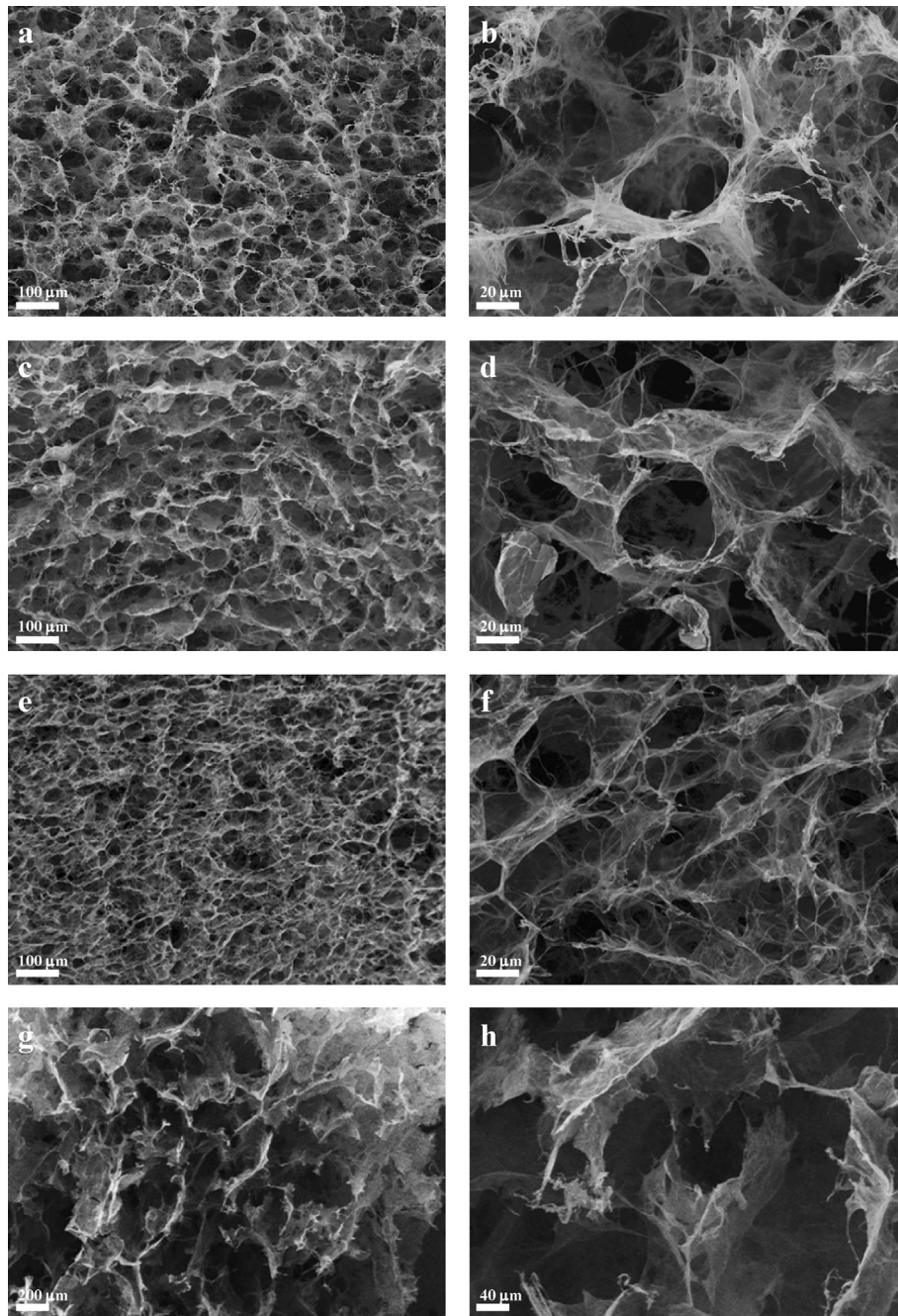


Fig. 4. The cross-sectional SEM images of (a, b) C0.3, (c, d) C0.6, (e, f) C0.9, (g, h) C0.6 powders.

3.4. The mechanism for the MA performance dependence on the composition and structure of the GF

Based on the general MA principle, the interfacial impedance gap and radiation energy loss ratio are regarded as the two critical factors that determine the material's MA performance [8,18,37,52]. To a typical single-layer dielectric MA material, such as graphene/polymer composites, the incident wave propagation from free space into the material is mainly affected by material's dielectric permittivity ϵ and electrical conductivity δ [4,37,39,53]. To better understand the MA performance dependence on their composition and morphology, we investigated various GFs' bulk electrical conductivities and relative permittivities in 2–18 GHz.

The electrical conductivities for all the GFs are shown in Fig. S2. It can be seen that the rise in either of the graphene volume fraction and the annealing temperature will result in the bulk electrical conductivity increase of the GF. The long-range induced currents decay on the conductive skeleton plays a key role in the substantially enhanced MA. The improved conductive graphene framework of the GF should couple with more time-varying electromagnetic fields within broader frequency bands and thus consume more radiation energy [32,37]. It's worth noting that even for C0.9 and T800, their bulk conductivities still stay below 1.0×10^{-4} S/m, which contributes to the good interfacial impedance matching and thus weakening adverse back reflection of microwave [9,22].

The real permittivity ϵ' responds to the storage capability of the

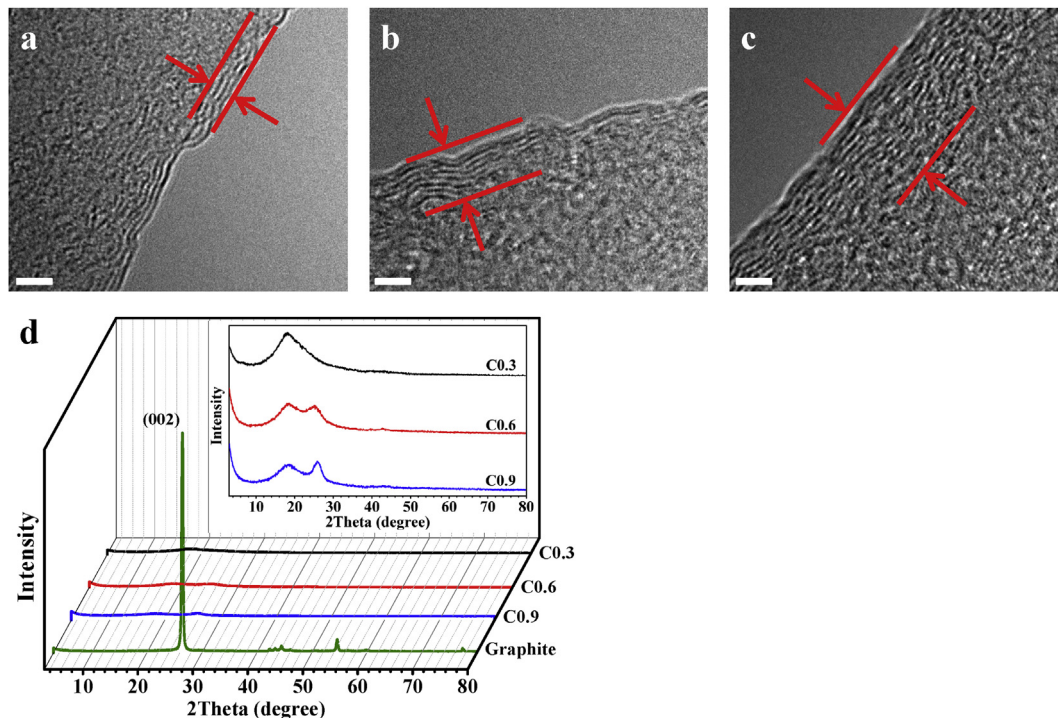


Fig. 5. The TEM images of the broken GF cell wall of (a) C0.3, (b) C0.6 and (c) C0.9 after sonication. (d) The XRD results of the GFs made from different initial GO solutions and flake graphite for comparison. The inset gives detailed patterns of three GF samples. (A colour version of this figure can be viewed online.)

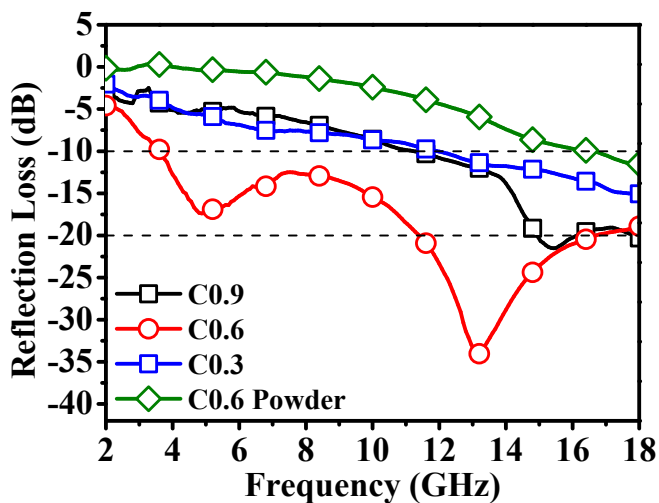


Fig. 6. The RL curves for the GFs with different physical structures are shown in 2–18 GHz. (A colour version of this figure can be viewed online.)

electric field inside the absorber [10,54], and a smaller ϵ' shortens the interfacial impedance gap, thus decreasing the reflection coefficient of the absorber [55]. In addition, the dielectric loss tangent ($\tan \delta_e = \epsilon''/\epsilon'$) represents the material's conversion of the microwave radiation into other energy forms [8,10]. The higher dielectric loss tangent, the more electromagnetic wave energy gets absorbed [9,11]. The inclination to any side wouldn't give rise to a good MA behavior [10,35]. Fig. 8 gives real permittivities and relative dielectric loss tangent values for all the GFs. Both T0 (Fig. 8a) and C0.3 (Fig. 8b) show very low real permittivities and dielectric loss tangents, which are even below those of single low-loss polymers such as poly(dimethyl siloxane) [51] and poly(ethylene oxide) [56].

It's clearly seen that both the real permittivity and dielectric loss tangent of the GF grow bigger monotonically with either the graphene volume fraction or reduction temperature increasing. The result, however, is not consistent with the MA performance change, which demonstrates the importance of the balance between the low permittivity and high dielectric loss to a satisfying microwave-absorbing ability. In all GF samples, the T800 and C0.9, though possessing the strong energy conversion abilities, exhibit over high real permittivity values, which goes against the well-matched impedance bridge and thus results in an attenuated MA property of the GF. By contrast, over low dielectric loss tangents of the GFs including C0.3, T0 and T200 due to sparse conductive networks and excessive defects of graphene sheets, reveal their poor microwave dissipation performance during the wave propagation from penetrating the foam to returning to the receiving antenna. The GF T600 or C0.6, with proper permittivity and high dielectric loss tangent, successfully build a win–win relationship between the interfacial matching and loss property, thus exhibiting the best MA performance. It should be noted that despite of ultralow real permittivity, the inferior dielectric loss tangent of the C0.6 powder suggests that both the ultrahigh porosity and tremendous long-range cross-linked conductive graphene network are imperative to the excellent MA performance of the GF.

To reflect the intrinsic MA mechanism more directly, we then simulated the RL curves for all the GFs. According to the transmission-line theory, the RL of electromagnetic wave radiation, R (dB), under normal wave incidence on a metal-backed single-layer MA material is correlated with the incident impedance Z_{in} as [8,56].

$$R(\text{dB}) = 20 \log \left| \frac{Z_{in} - Z_0}{Z_{in} + Z_0} \right| \quad (3)$$

where Z_0 is the characteristic impedance of free space (377Ω). Z_{in} is the input impedance at the interface of free space and the MA

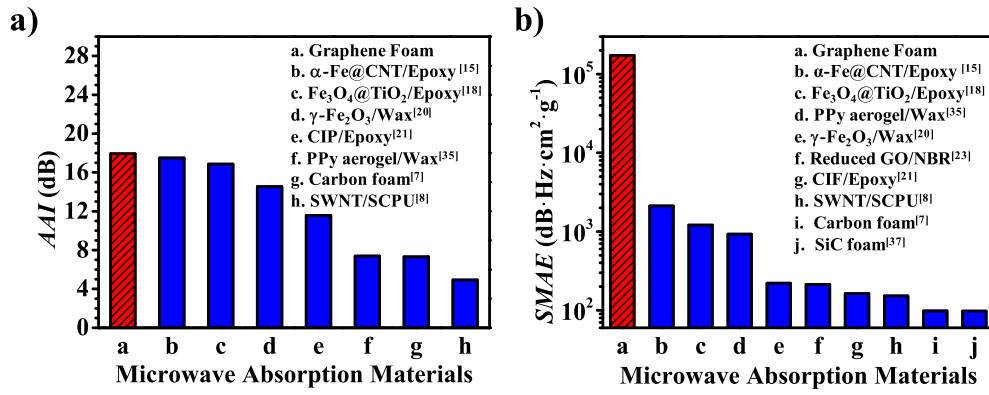


Fig. 7. Comparison of (a) AAI and (b) SMAE values for the GF (light grey patterned column) in this work and the representative materials (dark grey columns). More detailed data have been listed in Table S1 in the Supporting Information. (A colour version of this figure can be viewed online.)

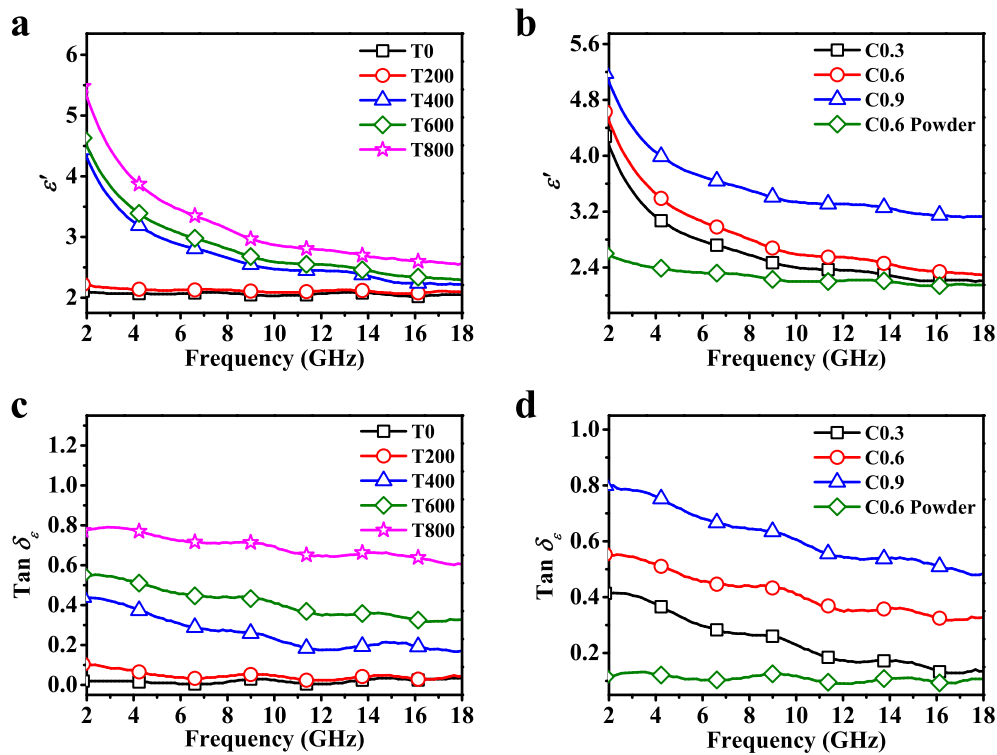


Fig. 8. Real parts of the complex permittivities of (a) the GFs with different chemical compositions and (b) the GFs with different physical structures in 2–18 GHz. Dielectric loss tangents of the GFs of (c) the GFs with different chemical compositions and (d) the GFs with different physical structures in 2–18 GHz. (A colour version of this figure can be viewed online.)

material, given as [20,35].

$$Z_{in} = Z_0 \sqrt{\frac{\mu_r}{\epsilon_r}} \tanh(2\pi f d \sqrt{\mu_r \mu_0 \epsilon_r \epsilon_0} j) \quad (4)$$

where f is the microwave frequency, d is the material thickness, ϵ_r is the relative permittivity and μ_r is the relative permeability.

The simulated MA curves in 2–18 GHz for all the GFs are shown in Fig. S3. The theoretical MA curves agree well with the experimental results in the aspect of the MA performance trend with initial GO concentration and thermal reduction temperature. For example, the calculated microwave absorbing property of the GF undergoes the same first rising and then falling change with the annealing temperature elevating from room temperature to 800 °C. However, the theoretical curve does not fit exactly on the measured

curve in the absorption performance and such discrepancy could be attributed to highly nonuniform porous structure inside the GF [57] and the edge effect of the GF junction in the MA test [21].

4. Conclusion

In summary, we have prepared series of GFs with various chemical compositions and physical structures by controlling the GO concentration of the initial solution and thermal-reduction temperature. The analyses of the GFs' compositions, structures and electromagnetic properties suggest that the MA performance of the GF is strongly correlated with the C/O ratio, conjugated carbon content and the graphene skeleton microstructure. A maximum absorption value of –34.0 dB as well as 14.3 GHz

qualified bandwidth can be achieved for the GF with an ultralow bulk density of 1.6 mg/cm^3 , which is close to the density of ambient air (1.2 mg/cm^3). Particularly, the GF present the best average absorption intensity compared with other typical MA materials in 2–18 GHz. The outstanding MA performance combined with an ultralow bulk density gives the GF a superior specific MA efficiency nearly two orders of magnitude higher than those of the best available MA materials reported before. The mechanism for the MA performance dependence on the composition and structure reveals that the GF with proper chemical composition and physical structure making the balance between excellent impedance matching and high loss characteristic could deliver an excellent MA property. With the facile and controllable synthesis of the GF, a new approach to efficiently optimize and regulate its MA behavior is now possible. More importantly, the processing–composition & structure–property relationships of the GF has opened up a new strategy to design rationally macroscopic porous materials for lightweight high-performance and broadband MA application such as the new-generation ultralight heat-resistant MA skin for high-speed aircrafts.

Acknowledgments

The authors gratefully acknowledge financial support from the MOST (Grants 2012CB933401), NSFC (Grants 21374050, 91433101, 51472124 and 51273093), MOE (B12015), PCSIRT (IRT1257) and NSF of Tianjin City (Grant 15JCYBJC17700).

Appendix A. Supplementary data

Supplementary data related to this article can be found at <http://dx.doi.org/10.1016/j.carbon.2016.04.070>.

References

- [1] X.J. Zhang, G.S. Wang, W.Q. Cao, Y.Z. Wei, J.F. Liang, L. Guo, et al., Enhanced microwave absorption property of reduced graphene oxide (RGO)-MnFe₂O₄ nanocomposites and polyvinylidene fluoride, *ACS Appl. Mater. Interfaces* 6 (10) (2014) 7471–7478.
- [2] Y. Chen, X. Liu, X. Mao, Q. Zhuang, Z. Xie, Z. Han, Gamma-Fe₂O₃-MWNT/poly(p-phenylenebenzobisoxazole) composites with excellent microwave absorption performance and thermal stability, *Nanoscale* 6 (12) (2014) 6440–6447.
- [3] H. Zhou, J. Wang, J. Zhuang, Q. Liu, A covalent route for efficient surface modification of ordered mesoporous carbon as high performance microwave absorbers, *Nanoscale* 5 (24) (2013) 12502–12511.
- [4] Z. Liu, G. Bai, Y. Huang, Y. Ma, F. Du, F. Li, et al., Reflection and absorption contributions to the electromagnetic interference shielding of single-walled carbon nanotube/polyurethane composites, *Carbon* 45 (4) (2007) 821–827.
- [5] A. Namai, S. Sakurai, M. Nakajima, T. Suemoto, K. Matsumoto, M. Goto, et al., Synthesis of an electromagnetic wave absorber for high-speed wireless communication, *J. Am. Chem. Soc.* 131 (3) (2008) 1170–1173.
- [6] S. Banik, S. Bandyopadhyay, S. Ganguly, Bioeffects of microwave – a brief review, *Bioresour. Technol.* 87 (2) (2003) 155–159.
- [7] J. Yang, Z.-m. Shen, Z.-b. Hao, Microwave characteristics of sandwich composites with mesophase pitch carbon foams as core, *Carbon* 42 (8) (2004) 1882–1885.
- [8] Z. Liu, G. Bai, Y. Huang, F. Li, Y. Ma, T. Guo, et al., Microwave absorption of single-walled carbon nanotubes/soluble cross-linked polyurethane composites, *J. Phys. Chem. C* 111 (37) (2007) 13696–13700.
- [9] X. Li, J. Feng, Y. Du, J. Bai, H. Fan, H. Zhang, et al., One-pot synthesis of CoFe₂O₄/graphene oxide hybrids and their conversion into FeCo/graphene hybrids for lightweight and highly efficient microwave absorber, *J. Mater. Chem. A* 3 (10) (2015) 5535–5546.
- [10] L. Wang, Y. Huang, X. Sun, H. Huang, P. Liu, M. Zong, et al., Synthesis and microwave absorption enhancement of graphene@Fe₃O₄@SiO₂@NiO nano-sheet hierarchical structures, *Nanoscale* 6 (6) (2014) 3157–3164.
- [11] H. Yang, M. Cao, Y. Li, H. Shi, Z. Hou, X. Fang, et al., Enhanced Dielectric Properties and Excellent Microwave Absorption of SiC Powders Driven with NiO Nanorings, *Adv. Opt. Mater.* 2 (3) (2014) 214–219.
- [12] D. Sun, Q. Zou, Y. Wang, W. Jiang, F. Li, Controllable synthesis of porous Fe₃O₄@ZnO sphere decorated graphene for extraordinary electromagnetic wave absorption, *Nanoscale* 6 (12) (2014) 6557–6562.
- [13] T. Liu, Y. Pang, M. Zhu, S. Kobayashi, Microporous Co@CoO nanoparticles with superior microwave absorption properties, *Nanoscale* 6 (4) (2014) 2447–2454.
- [14] N. Yousefi, X. Sun, X. Lin, X. Shen, J. Jia, B. Zhang, et al., Highly aligned graphene/polymer nanocomposites with excellent dielectric properties for high-performance electromagnetic interference shielding, *Adv. Mater.* 26 (31) (2014) 5480–5487.
- [15] R. Che, L.M. Peng, X.F. Duan, Q. Chen, X. Liang, Microwave absorption enhancement and complex permittivity and permeability of Fe encapsulated within carbon nanotubes, *Adv. Mater.* 16 (5) (2004) 401–405.
- [16] H. Zhang, J. Zhang, H. Zhang, Numerical predictions for radar absorbing silicon carbide foams using a finite integration technique with a perfect boundary approximation, *Smart Mater. Struct.* 15 (3) (2006) 759–766.
- [17] Y. Qing, W. Zhou, F. Luo, D. Zhu, Epoxy-silicone filled with multi-walled carbon nanotubes and carbonyl iron particles as a microwave absorber, *Carbon* 48 (14) (2010) 4074–4080.
- [18] J. Liu, R. Che, H. Chen, F. Zhang, F. Xia, Q. Wu, et al., Microwave absorption enhancement of multifunctional composite microspheres with spinel Fe₃O₄ Cores and Anatase TiO₂ shells, *Small* 8 (8) (2012) 1214–1221.
- [19] X. Shen, F. Song, J. Xiang, M. Liu, Y. Zhu, Y. Wang, et al., Shape anisotropy, exchange-coupling interaction and microwave absorption of hard/soft nanocomposite ferrite microfibers, *J. Am. Ceram. Soc.* 95 (12) (2012) 3863–3870.
- [20] G. Sun, B. Dong, M. Cao, B. Wei, C. Hu, Hierarchical dendrite-like magnetic materials of Fe₃O₄, γ-Fe₂O₃, and Fe with high performance of microwave absorption, *Chem. Mater.* 23 (6) (2011) 1587–1593.
- [21] W. Li, T. Wu, W. Wang, P. Zhai, J. Guan, Broadband patterned magnetic microwave absorber, *J. Appl. Phys.* 116 (4) (2014) 044110.
- [22] C.H. Gong, J.W. Zhang, C. Yan, X.Q. Cheng, J.W. Zhang, L.G. Yu, et al., Synthesis and microwave electromagnetic properties of nanosized titanium nitride, *J. Mater. Chem.* 22 (8) (2012) 3370–3376.
- [23] V.K. Singh, A. Shukla, M.K. Patra, L. Saini, R.K. Jani, S.R. Vadera, et al., Microwave absorbing properties of a thermally reduced graphene oxide/nitrile butadiene rubber composite, *Carbon* 50 (6) (2012) 2202–2208.
- [24] Z. Fan, G. Luo, Z. Zhang, L. Zhou, F. Wei, Electromagnetic and microwave absorbing properties of multi-walled carbon nanotubes/polymer composites, *Mater. Sci. Eng. B* 132 (1–2) (2006) 85–89.
- [25] T. Wang, H. Wang, X. Chi, R. Li, J. Wang, Synthesis and microwave absorption properties of Fe–C nanofibers by electrospinning with disperse Fe nanoparticles parceled by carbon, *Carbon* 74 (2014) 312–318.
- [26] G. Wang, Z. Gao, S. Tang, C. Chen, F. Duan, S. Zhao, et al., Microwave absorption properties of carbon nanocoils coated with highly controlled magnetic materials by atomic layer deposition, *ACS Nano* 6 (12) (2012) 11009–11017.
- [27] X. Chen, Y. Ye, J. Cheng, Recent progress in electromagnetic wave absorbers, *J. Inorg. Mater.* 26 (5) (2011) 449–457.
- [28] Y. Yang, M.C. Gupta, K.L. Dudley, R.W. Lawrence, Conductive carbon nanofiber–polymer foam structures, *Adv. Mater.* 17 (16) (2005) 1999–2003.
- [29] F. Moglie, D. Micheli, S. Laurenzi, M. Marchetti, V. Mariani Primiani, Electromagnetic shielding performance of carbon foams, *Carbon* 50 (5) (2012) 1972–1980.
- [30] Z. Chen, C. Xu, C. Ma, W. Ren, H.M. Cheng, Lightweight and flexible graphene foam composites for high-performance electromagnetic interference shielding, *Adv. Mater.* 25 (9) (2013) 1296–1300.
- [31] R. Kumar, S.R. Dhakate, T. Gupta, P. Saini, B.P. Singh, R.B. Mathur, Effective improvement of the properties of light weight carbon foam by decoration with multi-wall carbon nanotubes, *J. Mater. Chem. A* 1 (18) (2013) 5727–5735.
- [32] Y. Zhang, Y. Huang, T. Zhang, H. Chang, P. Xiao, H. Chen, et al., Broadband and tunable high-performance microwave absorption of an ultralight and highly compressible graphene foam, *Adv. Mater.* 27 (12) (2015) 2049–2053.
- [33] Z. Fang, X. Cao, C. Li, H. Zhang, J. Zhang, H. Zhang, Investigation of carbon foams as microwave absorber: numerical prediction and experimental validation, *Carbon* 44 (15) (2006) 3368–3370.
- [34] H. Huang, C. Liu, D. Zhou, X. Jiang, G. Zhong, D. Yan, et al., Cellulose composite aerogel for highly efficient electromagnetic interference shielding, *J. Mater. Chem. A* 3 (9) (2015) 4983–4991.
- [35] A. Xie, F. Wu, M. Sun, X. Dai, Z. Xu, Y. Qiu, et al., Self-assembled ultralight three-dimensional polypyrrole aerogel for effective electromagnetic absorption, *Appl. Phys. Lett.* 106 (22) (2015) 222902.
- [36] X.W. Zhu, D.L. Jiang, S.H. Tan, Microwave absorbing property of SiC reticulated porous ceramics, *J. Inorg. Mater.* 17 (6) (2002) 1152–1156.
- [37] H. Zhang, J. Zhang, H. Zhang, Computation of radar absorbing silicon carbide foams and their silica matrix composites, *Comput. Mater. Sci.* 38 (4) (2007) 857–864.
- [38] M. Inagaki, J. Qiu, Q. Guo, Carbon foam: preparation and application, *Carbon* 87 (2015) 128–152.
- [39] Y. Li, B. Shen, X. Pei, Y. Zhang, D. Yi, W. Zhai, et al., Ultrathin carbon foams for effective electromagnetic interference shielding, *Carbon* 100 (2016) 375–385.
- [40] M. Crespo, M. González, A.L. Elías, L. Pulickal Rajukumar, J. Basella, M. Terrones, et al., Ultra-light carbon nanotube sponge as an efficient electromagnetic shielding material in the GHz range, *Phys. Status Solidi RRL* 8 (8) (2014) 698–704.
- [41] X. Cao, Z. Yin, H. Zhang, Three-dimensional graphene materials: preparation, structures and application in supercapacitors, *Energy Environ. Sci.* 7 (6) (2014) 1850–1865.
- [42] Y. Wu, N. Yi, L. Huang, T. Zhang, S. Fang, H. Chang, et al., Three-dimensionally

- bonded spongy graphene material with super compressive elasticity and near-zero Poisson's ratio, *Nat. Commun.* 6 (2015) 6141.
- [43] Y. Li, J. Chen, L. Huang, C. Li, J.D. Hong, G. Shi, Highly compressible macroporous graphene monoliths via an improved hydrothermal process, *Adv. Mater.* 26 (28) (2014) 4789–4793.
- [44] Z. Xu, C. Gao, Graphene in macroscopic order: liquid crystals and wet-spun fibers, *Acc. Chem. Res.* 47 (4) (2014) 1267–1276.
- [45] J.J. Shao, W. Lv, Q.H. Yang, Self-assembly of graphene oxide at interfaces, *Adv. Mater.* 26 (32) (2014) 5586–5612.
- [46] C. Hu, X. Zhai, L. Liu, Y. Zhao, L. Jiang, L. Qu, Spontaneous reduction and assembly of graphene oxide into three-dimensional graphene network on arbitrary conductive substrates, *Sci. Rep.* 3 (2013) 2065.
- [47] Z. Chen, W. Ren, L. Gao, B. Liu, S. Pei, H.-M. Cheng, Three-dimensional flexible and conductive interconnected graphene networks grown by chemical vapour deposition, *Nat. Mater.* 10 (6) (2011) 424–428.
- [48] L. Zhang, F. Zhang, X. Yang, G. Long, Y. Wu, T. Zhang, et al., Porous 3D graphene-based bulk materials with exceptional high surface area and excellent conductivity for supercapacitors, *Sci. Rep.* 3 (2013) 1408.
- [49] W. Lv, C. Zhang, Z. Li, Q.H. Yang, Self-assembled 3D graphene monolith from solution, *J. Phys. Chem. Lett.* 6 (4) (2015) 658–668.
- [50] B. Wen, M. Cao, M. Lu, W. Cao, H. Shi, J. Liu, et al., Reduced graphene oxides: light-weight and high-efficiency electromagnetic interference shielding at elevated temperatures, *Adv. Mater.* 26 (21) (2014) 3484–3489.
- [51] L. Kong, X. Yin, X. Yuan, Y. Zhang, X. Liu, L. Cheng, et al., Electromagnetic wave absorption properties of graphene modified with carbon nanotube/poly(dimethyl siloxane) composites, *Carbon* 73 (2014) 185–193.
- [52] J. Jiang, D. Li, D. Geng, J. An, J. He, W. Liu, et al., Microwave absorption properties of core double-shell FeCo/C/BaTiO₃ nanocomposites, *Nanoscale* 6 (8) (2014) 3967–3971.
- [53] Y. Ren, C. Zhu, S. Zhang, C. Li, Y. Chen, P. Gao, et al., Three-dimensional SiO₂@Fe₃O₄ core/shell nanorod array/graphene architecture: synthesis and electromagnetic absorption properties, *Nanoscale* 5 (24) (2013) 12296–12303.
- [54] H. Sun, R. Che, X. You, Y. Jiang, Z. Yang, J. Deng, et al., Cross-stacking aligned carbon-nanotube films to tune microwave absorption frequencies and increase absorption intensities, *Adv. Mater.* 26 (48) (2014) 8120–8125.
- [55] V. Weston, Theory of absorbers in scattering, *IEEE Trans. Antennas Propag.* 11 (5) (1963) 578–584.
- [56] X. Bai, Y. Zhai, Y. Zhang, Green to prepare graphene-based composites with high microwave absorption capacity, *J. Phys. Chem. C* 115 (23) (2011) 11673–11677.
- [57] W.J. Hoefer, The transmission-line matrix method-theory and applications, *IEEE Trans. Microw. Theory Tech.* 33 (10) (1985) 882–893.